Synchrotron X-ray tomography for investigations of water distribution in polymer electrolyte membrane fuel cells

Ph. Krüger[a,*], H. Markötter[b], J. Haußmann[a], M. Klages[a], T. Arlt[b], J. Banhart[b], Ch. Hartnig[a,1], I. Manke[b], J. Scholta[a]

[a] Zentrum für Sonnenergie und Wasserstoff-Forschung Baden-Württemberg (ZSW), Helmholtzstraße 8, 89081 Ulm, Germany
[b] Helmholtz-Centre Berlin for Materials and Energy (HZB), Hahn-Meitner-Platz 1, 14109 Berlin, Germany

ARTICLE INFO

ABSTRACT

Synchrotron X-ray tomography is used to visualize the water distribution in gas diffusion layers (GDL) and flow field channels of a polymer electrolyte membrane fuel cell (PEMFC) subsequent to operation. An experimental setup with a high spatial resolution of down to 10 μm is applied to investigate fundamental aspects of liquid water formations in the GDL substrate as well as the formation of water agglomerates in the flow field channels. Detailed analyses of water distribution regarding the GDL depth profile and the dependence of current density on the water amount in the GDL substrate are addressed. Visualizations of water droplets and wetting layer formations in the flow field channels are shown. The three-dimensional insight by means of this quasi in situ tomography allows for a better understanding of PEMFC water management at steady state operation conditions. The effect of membrane swelling as function of current density is pointed out. Results can serve as an essential input to create and verify flow field simulation outputs and single-phase models.

© 2010 Elsevier B.V. All rights reserved.

1. Introduction

So far, tomographic visualizations of PEMFCs have been realized only by means of neutron radiation [1,2]. Two-dimensional visualization was proposed by several approaches applying modified cells with transparent parts [3–7]. Occurring interference with the water content set the limitations of this method. Also neutron radiography with around 50 μm spatial resolution was not suitable for a detailed view on the distribution of liquid water in the porous structure of the GDL substrate [8–14].

Synchrotron X-ray radiography was applied to detect liquid water in PEMFCs and bubble formations in direct methanol fuel cells (DMFC) with enhanced resolution of down to 1.5 μm per pixel [15–20]. From two different viewing directions an insight on the fuel cell processes in an operating system has been achieved. The in-plane view allowed distinguishing liquid water agglomerations in the GDL substrate and the flow field channels on the cathode and anode side. Transport pathways from the catalyst layer to the flow field channel could be observed. The through-plane viewing direction enables to analyze the liquid water generation process

in the GDL and differentiate between areas under the ribs and the channels and allows for detection of the eruptive water droplet formation in the flow field channels. Due to the two-dimensional information gained from the captured radiographs in combination of both viewing directions a pseudo-3D insight was received. However, for a precise localization of the liquid water distribution in the PEMFC tomographic investigations are needed to obtain real three-dimensional information.

The imaging method of synchrotron X-ray tomography has been applied up to now for ex situ material investigations. Based on data from ex situ GDL tomography the GDL and the micro porous layer (MPL) structure have been modelled [21] and have been used for further simulations activities. Synchrotron X-ray tomography with a resolution of 10 μm has been employed for ex situ studies on water content in gas diffusion media [22].

For the first time a three-dimensional insight has been gained on the water distribution in a PEMFC immediately after operation employing a fuel cell design fitted to synchrotron X-ray beamline boundary conditions. By means of synchrotron X-ray tomography even small water clusters can be localized very precisely inside a fuel cell resembling realistic operation conditions with regard to temperature and current densities. Droplet and layer formation in the flow field channels are shown and the content of small water agglomerations evolving in the gas diffusion layer is determined. In-plane views for membrane thickness measurements at defined steady state operating points are presented.

2. Instrumentation and experiment

2.1. Tomography setup

All experiments were run at the tomography facility of the BAM-line of the electron storage ring BESSY II at Helmholtz-Centre Berlin. A monochromatic synchrotron X-ray beam at an energy level of 15 keV was obtained by a W–Si multilayer monochromator with an energy resolution of about $\Delta E/E = 10^{-2}$. For image capturing a PCO camera was employed with a 4008×2672 pixel CCD-chip. A scintillator area of 19.2 mm $\times$ 12.8 mm was projected by a lens system, onto the CCD-chip leading to a pixel size of 4.8 μm.

So the used camera setup allows for a $4008 \times 4008 \times 2672$ voxel reconstruction via filtered back projection (FBP). Due to the beam geometry for the presented experiments $4008 \times 4008 \times 1501$ voxels were used which corresponds to 19.2 mm $\times$ 7.2 mm of the scintillator (Fig. 1).

The measurement time per image consists of approximately 1 s for exposure plus data readout of the captured tomography projections. A whole tomogram took around 60 min accordingly to 1800 angle projections for reconstruction by FBP. The fuel cell was positioned upright on a precision rotation table to capture projections at exact projection angles.

2.2. Fuel cell setup

For the experiment a fuel cell setup was designed for synchrotron X-ray tomography needs with an active area of approximate 12.5 cm^2, so that the test cell can be operated at realistic utilization rates. Since the visualization of the complete cell is beyond the limitations of the synchrotron X-ray beam size, only a cut-out of the cell was observed. To prevent artefacts by applying FBP reconstruction the dimension of this cut-out was customized to fit to the beam dimension. Reconstruction artefacts occur if parts of the tomographic object drift out of the synchrotron X-ray beam during projection capturing. The cut-out diagonal of the length and width is smaller than the beam width. With this fuel cell design and the applied camera and scintillator setup one third of the whole active area could be visualized (Fig. 2).

The fuel cell design was modified at the cut-out area for the three-dimensional imaging method. To ensure transmission of the synchrotron X-ray beam the anodic and cathodic aluminium end plates were divided and replaced by acrylic glass stiffening over the
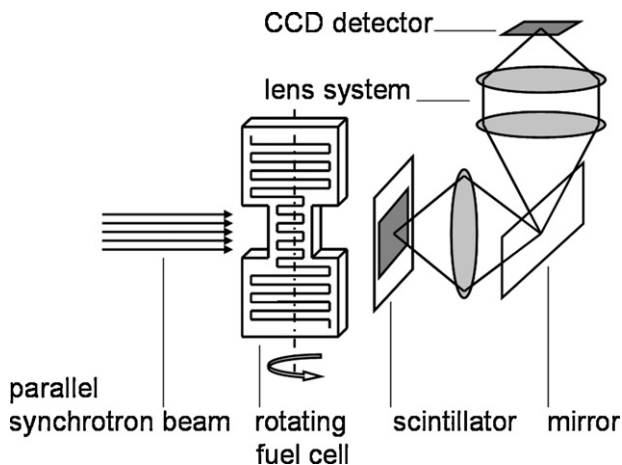

Fig. 1. Tomography setup for fuel cell investigations. The monochromatic synchrotron X-ray radiation transmits the PEM fuel cell at the cut-out. The inner cell assembly is projected on the scintillator screen and via a lens system detected by a 4008×2672 pixel CCD-Chip. Defined 180°-angle projections lead to a tomographic data set that is reconstructed by FBP to a three-dimensional tomogram.
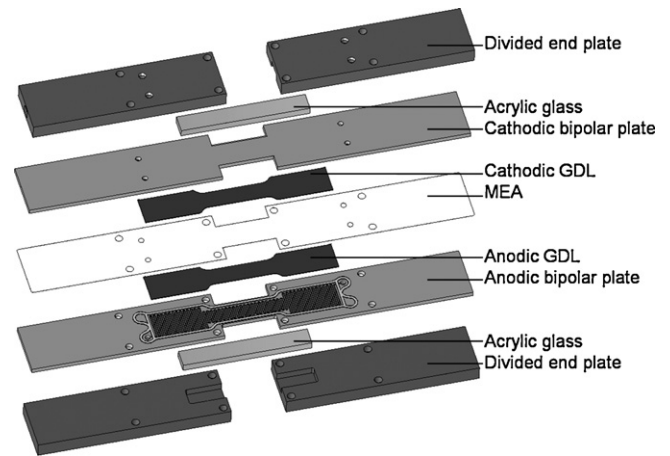

Fig. 2. Fuel cell stack assembly for tomographic imaging with a modified cut-out area in the middle of the active area. The anodic and cathodic end plates, which would absorb the synchrotron X-ray radiation completely, are divided and substituted by acrylic glass stiffeners. Also in in-plane direction the graphite composite bipolar plates are narrowing to prevent too much absorption during cell transmission.

cut-out area. An aluminium end plate of the given size would lead to complete absorption of the synchrotron X-ray radiation whereas acrylic glass has a negligible absorption rate. The mechanical function of the end plates, an equally distributed cell compression, has been ensured by this substitution. The fuel cell was designed without separate current collector plates. The load was directly connected to the end plates. The low electrical in-plane resistivity of the applied bipolar plate material of 90 μΩ m was sufficient to guarantee a uniform electrochemical activity across the complete active area. The stack temperature was controlled by heating cartridges.

A single channel serpentine gas flow field was machined in graphite composite with a channel width and depth of 0.5 mm and a rib width of 0.5 mm. It allowed to analyze liquid water distribution in the GDL and the channels and to distinguish easily between GDL areas under the ribs and under the channels regarding their water content. The flow field was surrounded by a seal channel. The sealing concept was construed as a hard-stop of a silicon seal string against the membrane. The GDL compression was defined by the inlay depth of 320 μm above the flow field channels via hard-stop which corresponds to a 400 μm GDL thickness at 80% compression. On both electrodes a SGL Carbon 10BC gas diffusion layer was applied coated with a MPL and a PTFE loading of 5 wt.% in the diffusion medium substrate.

A Nafion® 112 membrane with a thickness of 50 μm was applied. Due to the sealing concept the catalyst was only sprayed on the area which was provided as active area to ensure the sealing hard-stop against the non coated membrane around the active area. The electrodes consisted of a 40% Pt/C catalyst with loadings of 0.51 mg cm^{-2} on the anode and 0.57 mg cm^{-2} on the cathode.

The fuel cell was operated upright at standard parameter settings. The hydrogen stoichiometric ratio was set to 2.0, the air stoichiometric ratio to 2.5, at a stack temperature of $T = 50\,^\circ$C. The anodic and cathodic gas streams were unhumidified at all operation points. At the media outlets ambient pressure was kept. The polarisation curve and the power density curve of the employed fuel cell are shown in Fig. 3.

For tomographic investigations the fuel cell was operated from 40 mA cm^{-2} up to 160 mA cm^{-2} with increment steps of 40 mA cm^{-2}. The tomographies were started immediately after 15 min of steady state fuel cell operation. The water distribution was conserved by closing the gas inlets and outlets for the tomography.
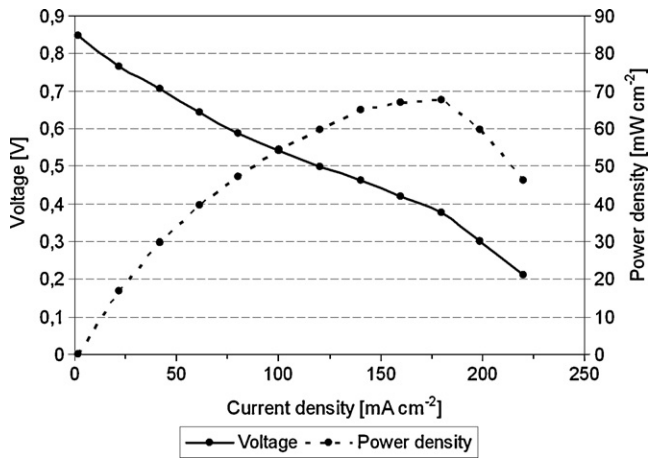
Fig. 3. Polarisation curve (solid line) and power density curve (dashed line) of the applied fuel cell. The hydrogen stoichiometric ratio was set to 2.0, the air stoichiometric ratio to 2.5. Maximum power output at $i = 180\,mA\,cm^{-2}$.
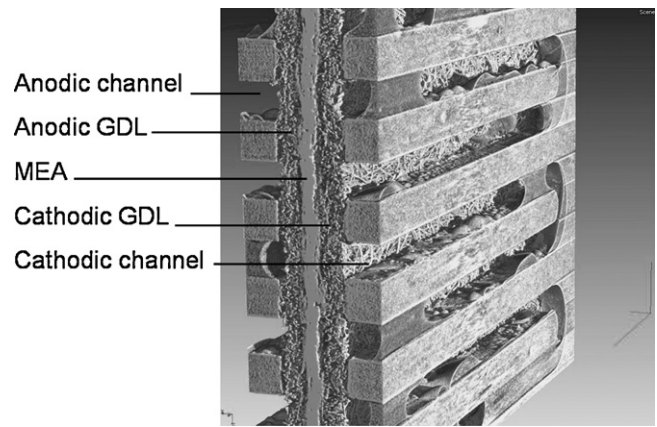

Fig. 4. Visualization of the tomographed fuel cell part. The cathode is shown on the front side, the anode on the back side of the 3D-image. Water films and separated droplets in the flow field channels could be visualized. The carbon fibre structure of the applied GDL is visible.

3. Results

As shown in Fig. 4, the water distribution could be visualized very precisely.

On the front side the water content of the cathodic flow field channels and the typical carbon fibre structure of the applied GDL can be observed. Water clusters are visible as wetting films or separated as small droplets on the cathode side; droplets on the anode side are mainly caused by back diffusion. Due to gravity water droplets are mainly formed on the bottom of the gas channel rib.

The analysis section-by-section allows for a detailed insight into the water distribution in each slice (Fig. 5).

During former measurement campaigns through-plane views were applied to detect water clusters in the GDL. The results were integral projections that showed the summarized water amount of the anode and cathode in the flow field channels and their GDL. In comparison the big advantage with the three-dimensional imaging is that one slice represents only a cell filament without showing cell components in front or behind the chosen slide. The thickness of a slice is due to the spatial resolution around 10 μm.

The water amount in the GDL depends on the fuel cell operation conditions and its specific structure and composition under operation. Determined by the interfaces GDL/channel and GDL substrate/MPL local variations and characteristics were observable. In Fig. 5 the water content in the cathodic GDL close to the flow field (B) was visualized at $i = 160\,mA\,cm^{-2}$. The water content of this section reflects the channel rib geometry.

The porous structures under the ribs were water-filled; the GDL areas under the channel were almost water-free at that slice position. This could be caused by two parallel effects: The compression of the GDL is higher under the ribs compared to under the channels of the flow field and the substrate can intrude into the channel. The pore size distribution under the ribs moves therefore to smaller pore diameters. This leads to a higher capillary pressure in these pores which counteracts the discharge of liquid water. The convective water discharge is obviously stronger under the channels and leads to almost no water agglomeration regarding the visualization in Fig. 5(B). The visualized water formations under the channel area at position (B) are connected with water cluster in the channel that protrude into the big pores of the substrate layer. These observations are in good agreement with simulated predictions [23].

A deeper insight in the GDL structure is allowed by the slices (C) which is in the middle of the diffusion layer between the transition
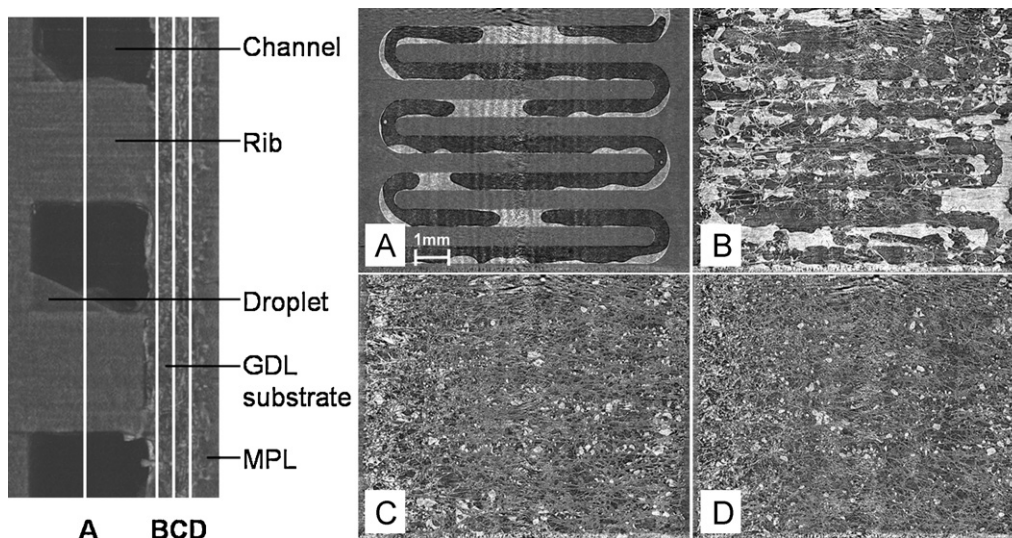

Fig. 5. Sketch with slide positions of the cathodic GDL. Section A is located in the flow field structure, sections B, C and D represent slices in the GDL substrate (left). Water agglomerations were visualized in each section and analyzed regarding the influencing parameters of the specific distribution.
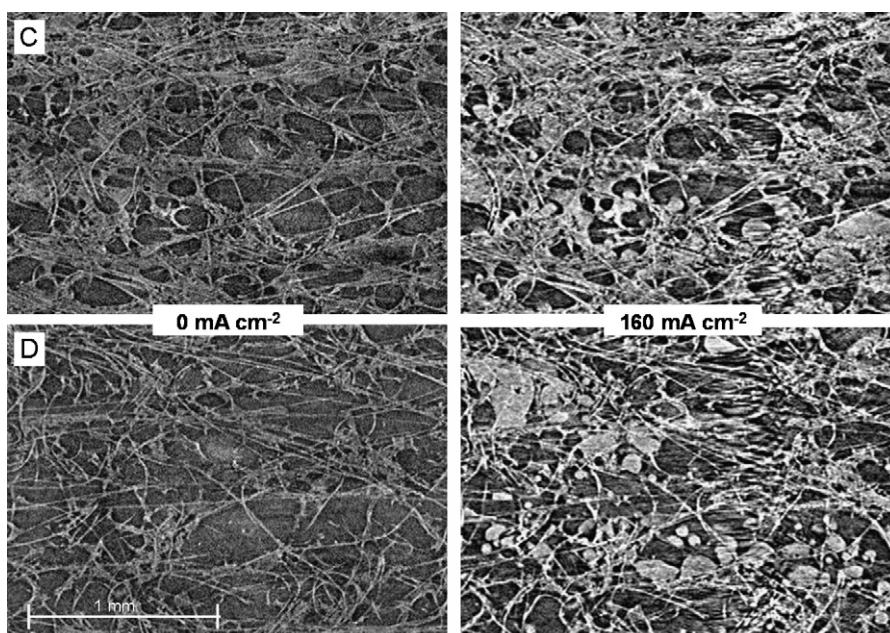
Fig. 6. Magnifications at position C and D of the GDL structure of the fuel cell. On the left side slices of the water-free tomogram at the same position are shown; for comparison on the right side slices of a tomogram at a current density at $i = 160\,\mathrm{mA\,cm^{-2}}$ with their correlating water content.

to the gas channels (B) and positions near to the MPL (D). An influence of the gas flow convection on the water distribution is only observable at the edge regions and at positions where water-filled pores exist over the whole GDL depth. The size of the water formations in the GDL substrate decreases at position (C) and (D), as shown in Fig. 6. The strong influence of the channel/rib assembly compared to position (B) is also not identifiable in these magnifications. The distribution of water in its liquid phase at positions closer to the catalyst layer is more related to the local pore geometry and the appearance of PTFE loading.

The obtained high resolution allows in addition for a morphologic separation of fibre material and binder/PTFE clusters: The visualization of the inhomogeneous structure of the GDL formed out of carbon fibres, binder and PTFE clusters is shown on the left side in Fig. 6.

A differentiation between binder and PTFE agglomerates is not possible. The water distribution and the adhesion of water clusters at carbon fibres are observable. The water amount is comparable at both positions.

The liquid water accumulation depends on current density which is best described by Faraday's law (Fig. 7).

At position B preferential spots were detected where initial water agglomerations appear and increase at a higher current density. Regarding to the large pores at this layer big water clusters span between crossing carbon fibres or fill larger holes in the GDL substrate.

The water clusters in layer D showed in the majority a drop form which indicates a higher local PTFE content at the slice position leading to higher contact angles. Furthermore it is possible at positions D that parts of the MPL protrude into the GDL substrate. In this
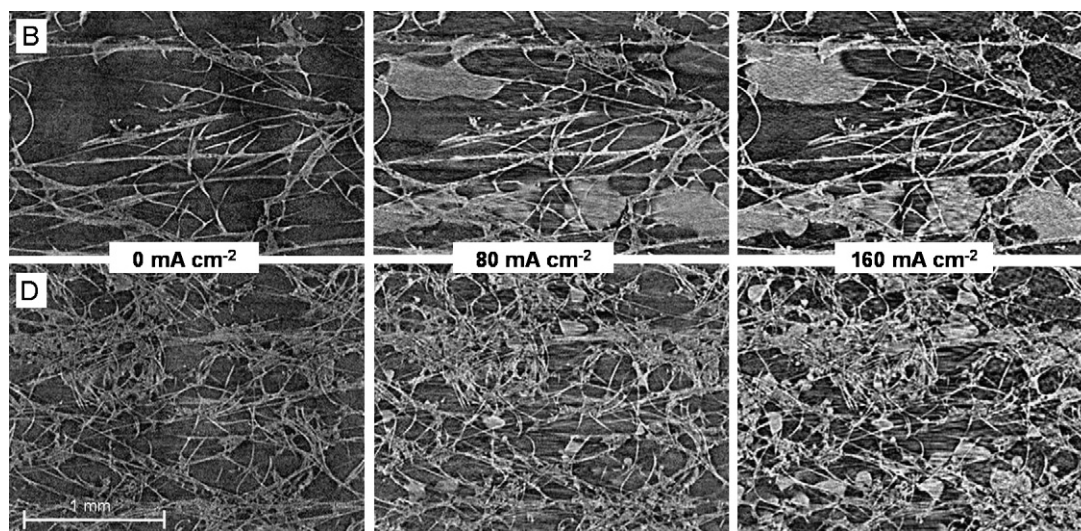

Fig. 7. Influence of the current density on the water amount at position B and D. The current density increases from $i = 0\,\mathrm{mA\,cm^{-2}}$ on the left side to $i = 80\,\mathrm{mA\,cm^{-2}}$ (middle) and finally to $i = 160\,\mathrm{mA\,cm^{-2}}$ on the right side; the water amount increases correlatively to the rising current density. The water formations depend on the local pore size distribution and PTFE loading (see text).
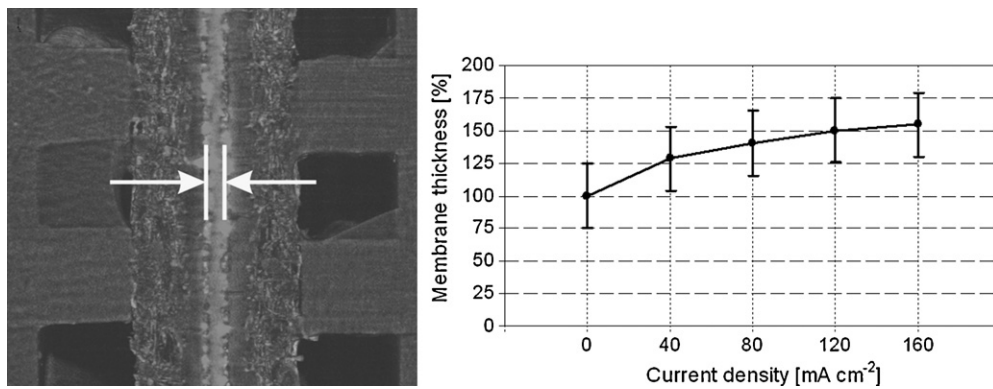
Fig. 8. Tomographic slice from in-plane viewing direction of membrane thickness measurements (left). The membrane thickness is averaged at each current density (right). The thickness was estimated at five different positions by calculating the number of pixels by means of the total pixel size from the detector setup.

case the water distribution and formation is besides the substrate PTFE loading influenced by the relatively higher PTFE content of the MPL. The influence of the current density on the water content is visible.

Corresponding to the analysis of the increasing water amount in the GDL structure the membrane thickness was estimated. With increasing current densities the membrane was intrinsically humidified. During operation the membrane swelled by accumulating product water from the cathodic catalyst layer. At $i = 160 \, \text{mA cm}^{-2}$ the membrane was swelled up to approximately 160% of the initial thickness. As shown in Fig. 8, the membrane thickness might reach saturation at higher current densities levels which were beyond the performance of the employed fuel cell.

4. Conclusion

Synchrotron X-ray tomography has been verified as a unique tool to investigate water distribution in operating fuel cells on a microscopic scale. A high-resolution three-dimensional insight has been generated which allows for analyzing the water content in the flow field channels, GDL substrate and MEA. The spatial resolution is sufficient to visualize microscopic water formations, carbon fibre structures under the flow field channels and ribs and to determine the membrane thickness as function of operating conditions. The chosen number of projections resulted in almost artefact-free three-dimensional reconstructions; lower projection rates would have led to a reduced signal-to-noise ratio.

The chosen concept of a fuel cell which was designed to synchrotron X-ray beamline boundary conditions while allowing for realistic operating conditions turned out to be reasonable to study the water content and the water distribution with tomographic resolutions. The employed fuel cell setup is the first design version for synchrotron X-ray tomography investigation. Further improvements might be necessary; the compression set worked as expected at the upper and lower fuel cell part compressed by the aluminium end plates. However, the substitution of the aluminium end plate by acrylic glass stiffeners in the central part led to slight convex deformation of the bipolar plates. This can potentially cause a reduced compression in the cut out area of the test cell. Nevertheless, the reached cell compression was sufficient for the presented investigations and analyses regarding water distribution aspects. The observed current densities, as displayed in the polarisation curve chart (Fig. 3), represent operation points when detectable water generation occur in the fuel cell assembly. The material thickness of the 50 μm Nafion® 112 membrane has facilitated to visualize membrane swelling. Performance losses caused by the membrane thickness were accepted to get new approaches in the field of MEA

investigations by means of synchrotron X-ray tomography.

The cell operation with unhumidified hydrogen and air ensured that the visualized water in the fuel cell assembly stemmed only from electrochemical processes. The captured water visualization in the diffusion media displays a snapshot of the transport process from the catalyst layer to the flow field channels. The influence of water discharge from the GDL via gas flow convection decreases over the substrate depth. Basically the water distribution is dependent on the depth profile of the GDL substrate and influenced by the local pore size distribution.

The formation of liquid water in the anodic and cathodic flow field channels has been visualized for steady state operation. The layer-wise analysis of the GDL substrate regarding to the water content is possible. The influence of the flow field geometry has been studied via the substrate depth profile and the local pore size distribution. The dependence of the water amount in the GDL on the applied current density has been visualized. Corresponding to effects on changes in current density the effect of membrane hydration has been rendered visible by measuring the membrane thickness.

For further investigations this non-destructive and non-invasive method could be employed for variations of MEA and GDL materials as well as different flow field designs. Their influences on the performance can be studied in more detail which opens a wide field for optimization of low temperature fuel cells. Material screenings of gas diffusion media regarding the water management or for analysis of degradation effects are possible targets. Variations in flow field designs can be analyzed with respect to gas flow properties and water discharge performance.

References

[1] I. Manke, Ch. Hartnig, M. Grünerbel, J. Kaczerowski, W. Lehnert, N. Kardjilov, A. Hilger, W. Treimer, M. Strobl, J. Banhart, Applied Physics Letters 90 (2007) 184101.
[2] D.S. Hussey, D.L. Jacobson, M. Arif, K.J. Coakley, D.F. Vecchia, Journal of Fuel Cell Science and Technology 7 (2010) 021024.
[3] S. Ge, C.-Y. Wang, Journal of the Electrochemical Society 154 (2007) 998–1005.
[4] F.Y. Zhang, X.G. Wang, C.-Y. Wang, Journal of the Electrochemical Society 153 (2006) 225–232.
[5] K. Tüber, D. Pócza, C. Hebling, Journal Power Sources 124 (2003) 403–414.

[6] P. Argyropoulos, K. Scott, W.M. Taama, Electrochimica Acta 44 (1999) 3575–3584.
[7] D. Spernjak, A.K. Prasad, S.G. Advani, Journal of Power Sources 170 (2007) 334–344.
[8] R. Satija, D.L. Jacobson, M. Arif, S.A. Werner, Journal of Power Sources 129 (2004) 238–245.
[9] A. Turhan, K. Heller, J.S. Brenizer, M.M. Mench, Journal of Power Sources 160 (2006) 1195–1203.
[10] A.B. Geiger, A. Tsukada, E. Lehmann, P. Vontobel, A. Wokaun, G.G. Scherer, Fuel Cells 2 (2002) 92–98.
[11] Ch. Hartnig, I. Manke, N. Kardjilov, A. Hilger, M. Grünerbel, J. Kaczerowski, J. Banhart, W. Lehnert, Journal of Power Sources 176 (2008) 452–459.
[12] I. Manke, Ch. Hartnig, N. Kardjilov, M. Messerschmidt, A. Hilger, M. Strobl, W. Lehnert, J. Banhart, Applied Physics Letters 92 (2008) 244101.
[13] P. Boillat, D. Kramer, B.C. Seyfang, G. Frei, E. Lehmann, G.G. Scherer, A. Wokaun, Y. Ichikawa, Y. Tasaki, K. Shinohara, Electrochemical Communications 10 (2008) 546.
[14] A.Z. Weber, M.A. Hickner, Electrochimica Acta 53 (2008) 7668–7674.
[15] Ch. Hartnig, I. Manke, R. Kuhn, N. Kardjilov, J. Banhart, W. Lehnert, Applied Physics Letters 92 (2008) 134106.
[16] Ch. Hartnig, I. Manke, R. Kuhn, S. Kleinau, J. Goebbels, J. Banhart, Journal of Power Sources 188 (2009) 468–474.
[17] I. Manke, Ch. Hartnig, M. Grünerbel, W. Lehnert, N. Kardjilov, A. Haibel, A. Hilger, H. Riesemeier, J. Banhart, Applied Physics Letters 90 (2007) 174105.
[18] I. Manke, C. Hartnig, H. Riesemeier, J. Goebbels, N. Kardjilov, R. Kuhn, P. Krüger, J. Banhart, Fuel Cells 10 (2010) 26–34.
[19] F. Büchi, R. Flückiger, D. Tehlar, F. Marone, M. Stampanoni, ECS Transactions 16 (2008) 587–592.
[20] Ch. Hartnig, I. Manke, J. Schloesser, Ph. Krüger, R. Kuhn, H. Riesemeier, K. Wippermann, J. Banhart, Electrochemistry Communications 11 (2009) 1559–1562.
[21] R. Thiedmann, Ch. Hartnig, I. Manke, V. Schmidt, W. Lehnert, Journal of the Electrochemical Society 156 (2009) B1339–B1347.
[22] P.K. Sinha, P. Halleck, C.-Y. Wang, Electrochemical and Solid-State Letters 9 (2006) A344–A348.
[23] A.A. Kulikovsky, T. Wuester, A. Egmen, D. Stolten, Journal of the Electrochemical Society 152 (2005) A1290–A1300.